molecular pharmaceutics

pubs.acs.org/molecularpharmaceutics



Article

# TRIPODD Enables Single-Cell Quantification of Therapeutic Efficacy

Nathan P. McMahon,[▽] Allison Solanki,[▽] Antonio R. Montaño, E. Sila Ozdemir, Kimberley S. Samkoe, Kenneth M. Tichauer, Lei G. Wang, and Summer L. Gibbs*

Cite This: *Mol. Pharmaceutics* 2026, 23, 1572−1585

Read Online

ACCESS | Metrics & More | Article Recommendations | Supporting Information

**ABSTRACT:** Targeted, small-molecule therapeutics have improved patient survival across cancer types, with >20 tyrosine kinase inhibitors (TKIs) receiving FDA approval as cancer therapies. While the initial TKI response is often promising, it is typically transient due to tumor evolution and subsequent therapeutic resistance driven by primary or acquired resistance mechanisms. While resistance mechanisms vary, there are currently no spatially resolved methodologies that provide a quantitative, mechanistic understanding of drug delivery and therapeutic response across therapeutic modalities (e.g., chemotherapy, radiotherapy, TKIs, immunotherapy) to enable personalized cancer therapy. Herein, we utilize our previously reported fluorescence imaging platform, **T**herapeutic **R**esponse **I**maging through **P**roteomic and **O**ptical **D**rug **D**istribution (**TRIPODD**), which is a quantitative protocol capable of interpreting the relationship between drug delivery and therapeutic response within the spatial context of a tumor to evaluate single-cell response and resistance to epidermal growth factor receptor TKI therapy. In this study, we applied TRIPODD to quantify the therapeutic response of EGFR-TKI-sensitive nonsmall cell lung cancer (NSCLC) xenografts to erlotinib, as a proof of concept for the platform. Through these studies, we were able to identify unique signatures of therapeutic response linked to the accumulation and engagement of erlotinib on a single-cell basis, demonstrating the utility of our TRIPODD platform technology in evaluating the treatment response and resistance at the single-cell level in heterogeneous tumors.

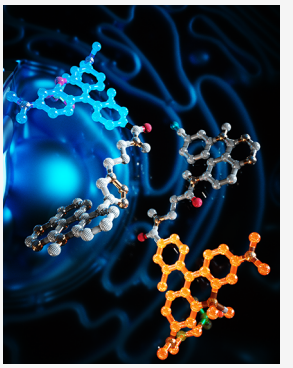

**KEYWORDS:** *intracellular paired agent imaging, fluorescence imaging, drug target availability, cyclic immunofluorescence, cancer heterogeneity*

## INTRODUCTION

The discovery and advancement of targeted, small-molecule therapeutics have improved patient survival across cancer types. Enthusiasm for molecularly targeted therapy is demonstrated by the Food and Drug Administration's (FDA) approval of >20 tyrosine kinase inhibitors (TKIs), a class of small-molecule therapeutics, for the treatment of numerous cancers.[1] However, while initial response in patients treated with TKIs is often promising, it is also typically transient due to tumor evolution and subsequent therapeutic resistance driven by primary or acquired resistance mechanisms.[2] One potential acquired resistance mechanism is the temporal and spatial variation in blood flow, impacting drug delivery both directly into a tumor and in its surrounding tumor microenvironment (TME). Abnormal vasculature is a recognized phenotype of solid tumors, resulting in impaired blood supply and increased tumor interstitial pressure.[3,4] These phenomena can result in hypoxic conditions that promote genetic instability and may prevent antitumor immune activity while also limiting therapeutic delivery and therefore efficacy.[5] TME modulation strategies are under investigation to increase tumor drug penetration and improve drug delivery to its target. For example, the inhibition of vascular endothelial growth factor (VEGF-A) has demonstrated the ability to renormalize vasculature in various solid tumor types.[6,7] However, there are currently no spatially resolved methodologies that provide a quantitative, mechanistic understanding of drug delivery and therapeutic response across treatment modalities (e.g., chemotherapy, radiotherapy, TKIs, and immunotherapy) to enable personalized cancer therapy.

We have previously reported a fluorescence imaging platform, **T**herapeutic **R**esponse **I**maging through **P**roteomic and **O**ptical **D**rug **D**istribution (**TRIPODD**),[8,9] which is a quantitative protocol capable of interpreting the relationship between drug delivery and therapeutic response within the spatial context of a tumor. TRIPODD concomitantly provides single-cell quantification of drug presence and spatial proteomic therapeutic response through the combination of two complementary technologies: intracellular paired agent imaging (iPAI) and oligonucleotide-conjugated antibody (Ab-oligo) cyclic immunofluorescence (cyCIF).[10−13] To account for off-target drug accumulation, iPAI utilizes a combination of spectrally distinct, fluorescently labeled targeted and control (untargeted) TKI drug derivative imaging agents to measure

**Received:** August 19, 2025
**Revised:** December 5, 2025
**Accepted:** December 5, 2025
**Published:** February 17, 2026

drug target availability (DTA).[13] To account for nonspecific drug accumulation that often obfuscates quantitative molecular cancer imaging due to variable enhanced permeability and retention (EPR) effects,[14] the ratio of the targeted to the untargeted agent enables assessment of drug uptake and retention (i.e., DTA). When the targeted agent is administered at a "trace" level (i.e., <5% of target sites are occupied by the targeted agent), the resulting value can be shown to be proportional to the concentration of targets available for binding.[15,16] We have previously established that as the concentration of the administered parent drug increases, DTA will decrease, as potential drug-binding sites are occupied by the parent drug administered therapeutically.[8,13] Importantly, the iPAI probes have a similar binding affinity to their parent drug and are intended only for DTA quantification after completion of treatment with the parent drug. The iPAI technique is, therefore, capable of assessing spatially resolved DTA heterogeneity across tumor tissues.

Therapeutic response can be linked to DTA using cyCIF performed on the same tissue sample from which iPAI was quantified. The cyCIF-defined spatial proteome can characterize treatment response mechanisms at the single-cell level, such as perturbed cell signaling, pro- or antiapoptotic signatures, and patterns of immune cell recruitment, phenotype, and localization within the TME.[17−24] Previously, we have demonstrated the feasibility of collecting both iPAI and cyCIF imaging data on the same tissue section using our DNA barcoded cyCIF methodology (i.e., Ab-oligo cyCIF), as proof-of-concept for the TRIPODD platform.[8] We have also shown the flexibility of the Ab-oligo cyCIF methodology for integration with a variety of immunofluorescence techniques[10] and have developed novel fluorophore technology (i.e., OregonFluor probes) optimized for iPAI in live cells and tissues.[13] Herein, we report on the first use of the TRIPODD platform to evaluate the therapeutic response in tumors dosed longitudinally with clinically approved therapeutics. In the current study, we applied the TRIPODD platform to quantify therapeutic response of epidermal growth factor (EGFR)-TKI-sensitive nonsmall cell lung cancer (NSCLC) xenografts to erlotinib, a first-generation EGFR TKI, treatment using a limited cyCIF-staining panel to quantify EGFR, phosphorylated EGFR, and cell state (i.e., proliferation and apoptosis). Using the TRIPODD platform, we were able to identify unique signatures of therapeutic response linked to accumulation and engagement of erlotinib on a single-cell basis, demonstrating the utility of our platform technology to evaluate treatment response and resistance at the single-cell level in heterogeneous tumors.

## MATERIALS AND METHODS

### iPAI Probe Synthesis

The targeted and untargeted (control) intracellular paired agent imaging (iPAI) agents were derivatives of erlotinib (Erl), a first-generation, reversible TKI targeting EGFR. Briefly, site selection for the synthesis of erlotinib derivates to generate targeted and untargeted drug imaging agents was guided by the structure of the parent drug bound to the EGFR crystal structure.[12,13] Our novel OregonFluors (OF), OF550 and OF650, were selected for agent labeling due to their spectral separation, overall charge, charge distribution, molecular weight, structural similarity, and stability in varied biological environments.[13] OF550 has maximum excitation and emission peaks at 552 and 575 nm, respectively. OF650 has maximum excitation and emission peaks at 649 and 668 nm, respectively. This novel class of rhodamine derivatives enables maintained biodistribution similarity between the targeted and untargeted agents, with stable fluorescence emission in varied biological environments.[13] OF550 and OF650 were used as labels to synthesize cell membrane-permeant targeted (T) and untargeted (UnT) iPAI agents, resulting in four unique probes: (1) $OF550_{Erl(T)}$, (2) $OF650_{Erl(T)}$, (3) $OF550_{Erl(UnT)}$, and (4) $OF650_{Erl(UnT)}$.

### Cell Lines

The human NSCLC cancer cell line HCC827, containing the exon 19 deletion EGFR mutation, used in this study was purchased from ATCC (Manassas, VA). The HCC827 cell line was selected due to its therapeutic sensitivity to EGFR TKIs.[25,26] The HCC827 cells were maintained at passage numbers <25 throughout experimentation and were regularly tested for mycoplasma contamination. The HCC827 cell line was expanded in Roswell Park Memorial Institute (RPMI) 1640 medium (Thermo Fisher Scientific, Waltham, MA) containing 10% fetal bovine serum (FBS) and 1% penicillin/streptomycin/glutamine (Thermo Fisher Scientific) and grown in a 37 °C, 5% $CO_2$ incubator.

### In Silico Molecular Dynamics Studies of Erlotinib and iPAI Agents

In silico molecular dynamics (MD) studies were conducted to assess the binding of erlotinib and iPAI erlotinib agents to the EGFR protein. The crystal structure of EGFR in complex with erlotinib has been previously reported.[27] MolView (molview.org), an open-source tool, was used to obtain the structures for the four iPAI agents ($OF550_{Erl(T)}$, $OF650_{Erl(T)}$, $OF550_{Erl(UnT)}$, and $OF650_{Erl(UnT)}$). AutoDock Vina (version 1.1.2, Linux) was used to model the docking of erlotinib and iPAI erlotinib agents to EGFR.[28] Hydrogen atoms were added to all receptors, and grid box dimensions were defined specific to the size of the receptor-binding pockets or interfaces. All-atom AMBER-type force-field parameters were generated for the four iPAI agents and the parent erlotinib. AMBER tools were used to generate gromacs-type force fields for the protein−drug complexes[29] and calculate partial charges at HF/6-31G (AM1-BCC).[30] The General AMBER Force Field (GAFF)[31] was used to calculate the bonded and van der Waals interactions in the appropriate molecular protonation state. A total of six initial configurations—EGFR alone, EGFR + erlotinib, EGFR + $OF650_{Erl(T)}$, EGFR + $OF650_{Erl(UnT)}$, EGFR + $OF550_{Erl(UnT)}$, and EGFR + $OF650_{Erl(UnT)}$—were simulated for 100 ns using the GROningen MAchine for Computer Simulations (GROMACS-2018) on a cloud computing cluster at Oregon Health and Science University (OHSU, Portland, OR). MD simulations were carried out in an aqueous environment. The TIP3P water model was used to solvate the system in an aqueous environment, with counterions ($Na^+$ or $Cl^-$) added to ensure charge neutrality. A 3D periodic box was used to center the complex within at least 1 nm of the edge, accounting for >2 nm of solvent buffer. The equilibration and production runs were completed in an isothermal−isobaric (NPT) ensemble, where the temperature was maintained at 300 K and the pressure was maintained at 1 bar using a V-rescale thermostat[32] and a Parrinello−Rahman barostat, respectively. The MD simulations employed a leapfrog algorithm with a 2 fs time step to integrate the equations of motion. The long-ranged electrostatic interactions were


https://doi.org/10.1021/acs.molpharmaceut.5c01220
Mol. Pharmaceutics 2026, 23, 1572−1585

calculated using the particle mesh Ewald (PME)[33] algorithm with a real-space cutoff of 1.2 nm. Lennard−Jones (LJ) interactions were also truncated at 1.2 nm. Root-mean-square deviations (RMSDs) of the complex structures were calculated as a function of time to monitor when the systems reached equilibration. To study the fluctuations in EGFR residues upon interaction with different probes, the RMSF was calculated using GROMACS functions as follows.

The average binding free energy was derived from the Gibbs free energy, $G$

$$G = E_{bnd} + E_{el} + E_{vdW} + G_{pol} + G_{apol} - TS \quad (1)$$

$$G = G_{MM} + G_{pol} + G_{apol} - TS \quad (2)$$

where $G_{MM}$, $G_{pol}$, and $G_{apol}$ represent the molecular mechanics, polar, and apolar contributions, respectively.[34] $E_{bnd}$ represents the bond energy, $E_{el}$ represents the electrostatic energy, and $E_{vdW}$ represents the van der Waals energy. The entropic contribution (TS) was not included in our calculations. The GROMACS *g_mmpbsa* package was used to obtain the $G_{MM}$, $G_{pol}$, and $G_{apol}$ contributions.[35,36] This package allowed the user to define the protein and ligand during the calculation and measure the average binding free energy between the ligand and protein, $\Delta G$, as follows

$$\Delta G = G^{complex} - (G^{protein} + G^{ligand}) \quad (3)$$

where $G^{complex}$ represents the free energy of the ligand−protein complex, $G^{protein}$ represents the free energy of the protein in its unbound state, and $G^{ligand}$ represents the free energy of the ligand in its unbound state.

### In Vitro iPAI Studies

Cells were plated in phenol-red-free media at a density of $1 \times 10^5$ cells/ml (100 $\mu$L/well) in 96-well glass-bottomed cell culture plates. After equilibrating cells for 24 h at 37 °C and 5% $CO_2$, cells were stained with Cetuximab (Eli Lilly and Co., Indianapolis, IN) that was directly conjugated to Alexa Fluor 488 (AF488, Thermo Fisher Scientific, final concentration = 5 $\mu$g/mL with a dye-to-protein ratio of 3.3) for 45 min at 37 °C and at 5% $CO_2$, followed by brief rinsing in prewarmed phosphate-buffered saline (PBS). iPAI-targeted agents ($OF650_{Erl(T)}$ and $OF550_{Erl(T)}$) and iPAI control agents ($OF550_{Erl(UnT)}$ and $OF650_{Erl(UnT)}$) were applied to distinct cells at the following equal molar concentrations: paired targeted agents at 250 nM; and paired control agents at 2 $\mu$M. iPAI agents were allowed to incubate for 1 h at 37 °C and 5% $CO_2$. The media in all wells were briefly washed five times with 100 $\mu$L per wash using phenol-red-free media and then replaced with fresh media prior to imaging on a Zeiss AxioObserver (Carl Zeiss AG, Oberkochen, Germany) modified with a Yokogawa CSU-X1 spinning disk confocal unit outfitted with a 20x-0.8 PlanApo objective. The following exposure times and excitation (x) and emission (m) filter combinations were utilized for image collection: AF488 at 2000 ms, 470/40x, 525/50m; OF550 at 2000 ms, 550/25x, 605/70m; and OF650 at 2000 ms, 640/30x, 690/50m.

### MTS Assay Validation

To determine the in vitro half-maximal inhibitory concentration ($IC_{50}$), cells were trypsinized, counted, and plated in 96-well glass-bottomed cell culture plates (Cellvis, Mountain View, CA) at a density of $5 \times 10^4$ cells/ml (100 $\mu$L/well). Cells were allowed to adhere and equilibrate overnight at 37 °C and 5% $CO_2$. The culture medium was then replaced with increasing concentrations of the parent drug, $OF650_{Erl(T)}$, or $OF550_{Erl(UnT)}$ (0−10 $\mu$M) and allowed to incubate at 37 °C and 5% $CO_2$. After 72 h, 20 $\mu$L of the MTS CellTiter 96 $AQ_{ueous}$ One Solution Cell Proliferation Assay Reagent (Promega, Madison, WI) was added to each well and gently mixed. The cells were incubated for an additional 3 h at 37 °C with 5% $CO_2$. The plates were read for absorbance at 490 nm (SpectraMax M5, Molecular Devices, Sunnyvale, CA). The wells containing only media were used as a positive (untreated) control for cell viability signal, and cells permeabilized with 0.1% Triton-X served as a negative control. GraphPad Prism (La Jolla, CA) was used to analyze the resulting dose−response curves.

### Kinase Binding Assay

In vitro binding affinity was evaluated for the fluorescently labeled EGFR iPAI agents and parent erlotinib using the Z'-LYTE kinase assay via the Thermo Fisher Scientific SelectScreen Kinase Profiling Service. Briefly, the individual compounds were screened over a titration curve starting at 10 $\mu$M against purified EGFR and the associated Tyr04 fluorescent ligand. The resulting inhibition behavior was analyzed by using GraphPad Prism.

### In-Cell Western Assay

HCC827 cells were seeded at $4 \times 10^4$ cells/well into a black-walled 96-well plate (Greiner) using culture media and incubated overnight at 37 °C and 5% $CO_2$. The cells were then incubated with either parent erlotinib (0−5 $\mu$M), $OF650_{Erl(T)}$ (0−50 $\mu$M), or $OF550_{Erl(UnT)}$ (0−50 $\mu$M) for 24 h. Control cells were treated with human epidermal growth factor (GE Biosciences, Piscataway, NJ) at 100 ng/mL for 30 min at 37 °C and 5% $CO_2$ prior to the initiation of the in-cell western assay. After incubation and between each of the following steps, the wells were washed three times with Dulbecco's phosphate-buffered saline (DPBS) containing $Mg^{2+}$ and $Ca^{2+}$. Cells were fixed in a 4% paraformaldehyde (PFA) solution for 15 min, permeabilized with 0.1% Triton-X-100 in PBS containing $Mg^{2+}$ and $Ca^{2+}$ for 45 min, and blocked with intercept blocking buffer for 1 h at room temperature. The cells were incubated with primary anti-EGFR (Thermo Fisher Scientific) and anti-pEGFR (Cell Signaling Technology, Danvers, MA) antibodies overnight at 4 °C. Wells were subsequently incubated with IRDye 800CW-labeled goat antimouse and VRDye 490-labeled goat antirabbit IgG secondary antibodies at room temperature for 2 h. After washing, 100 $\mu$L of DPBS containing $Mg^{2+}$ and $Ca^{2+}$ was added to each well for imaging. The plate was scanned on Odyssey M (LI-COR Biosciences, Lincoln, NE) using the plate scanning function in the 488 and 800 nm channels, and the mean fluorescence of each well was determined using Empiria Studio (LI-COR Biosciences).

### Animal Care and Use

All animal experiments were approved by the OHSU Institutional Animal Care and Use Committee (IACUC) and conducted under approved protocol TR04_IP00000202. Mice were housed in an OHSU vivarium, an IACUC and AAALAC-approved facility, and were inspected daily and supplied with standard food and water to ensure that they were not in pain or distress throughout the duration of the experiments. At least 1 week prior to tumor resection, mice were placed on a chlorophyll-free diet (Animal Specialties, Inc., Hubbard, OR). All rodent surgical procedures were carried out under full


https://doi.org/10.1021/acs.molpharmaceut.5c01220
Mol. Pharmaceutics 2026, 23, 1572−1585

anesthesia, utilizing a 90/10 mixture of ketamine/xylazine. Ketamine (Hospira Inc., Lake Forest, IL) was administered at a dose of 100 mg/kg, and xylazine (AnaSed, Shenandoah, IA) was administered at a dose of 10 mg/kg by intraperitoneal (IP) injection. The toe pinch method confirmed the depth of anesthesia and ensured a lack of reactivity prior to the commencement of any surgical procedures. Mice euthanasia was initiated by standard carbon dioxide inhalation under full anesthesia at the end of each experiment. Euthanasia of all mice was confirmed by physical examination to ensure that heartbeat and respiration had ceased. This method of euthanasia is humane, rapid, and consistent with the recommendations of the Panel on Euthanasia of the American Veterinary Medical Association.

### Mouse Xenograft Models

Athymic nude mice (Homozygous 490, Charles River Laboratories, Wilmington, MA) were implanted with HCC827 cells to generate a cell line-derived xenograft (CDX) model for in vivo erlotinib dosing studies. Cultured cells were first trypsinized and resuspended in RPMI phenol-red-free media without serum to a concentration of $3 \times 10^7$ cells/ml. Cells were implanted into the rear flanks of anesthetized mice at a final concentration of $1.5 \times 10^6$ cells/flank in 50% (v/v) Matrigel (Corning Inc., Corning, NY), resulting in two tumors per mouse. A total of two athymic nude mice were implanted for two cohorts included in an in vivo competitive binding study: iPAI agent ($OF650_{Erl(T)}$ and $OF550_{Erl(UnT)}$) injected mice or iPAI agent ($OF650_{Erl(T)}$ and $OF550_{Erl(UnT)}$) plus parent erlotinib injected mice. A total of $n = 12$ athymic nude mice were implanted for two dosing cohorts: one for erlotinib treatment and one for control mice without erlotinib treatment. Mice were monitored daily after implantation for tumor growth and body weight. Tumor growth was recorded every 3 days until tumors reached ∼300 $mm^3$.

### In Vivo Competitive Binding

HCC827 xenograft-bearing mice were systemically administered parent erlotinib via tail vein injection 24 h prior to systemic administration of equivalent doses of parent erlotinib and $OF650_{Erl(T)}$ and $OF550_{Erl(UnT)}$ (all at 2.5 mg/kg) 4 h prior to mouse euthanasia and tumor resection. The resected tumor tissues were immediately frozen in optimal cutting temperature compound (OCT; Fisher Scientific, Hampton, NH) in blocks prior to sectioning at a thickness of 10 $\mu$m. Tissue sections were subsequently imaged on a Zeiss AxioScan.Z1 slide scanner (detailed below) using the Cy2 channel (for autofluorescence focal map generation), Cy3 channel (for $OF550_{Erl(UnT)}$), and Cy5 channel (for $OF650_{Erl(T)}$). After image acquisition, a custom MATLAB script was used to calculate DTA images on a per-pixel basis for each tissue image.[8,9] DTA was calculated as

$$\text{drug target availability (DTA)} = \alpha \frac{I_T}{I_{UT}} \quad (4)$$

where $I_T$ represents the signal from the targeted agent $OF650_{Erl(T)}$, $I_{UT}$ represents the signal from the untargeted agent $OF550_{Erl(UnT)}$, and $\alpha$ represents a scaling factor to account for the signal intensity difference between the target and untargeted agents caused by collection in their respective fluorescence imaging channels. The scaling factor was determined by imaging the stock-injected solutions of targeted and untargeted agents at titrated concentrations on the Zeiss AxioScan.Z1 to generate linear calibration trend lines for each agent, where the ratio of the slope of the untargeted agent trend line to the slope of the targeted agent trend line was defined as the scaling factor. DTA for each tissue section was quantified by calculating the tissue mean DTA through manual segmentation of the tissue using ImageJ version 1.51 (National Institutes of Health, Bethesda, MD) and extracting the mean DTA from the tissue sections. The mean fluorescence signal or DTA value from each section was divided by the highest mean fluorescence or DTA value, respectively, to calculate the relative fluorescence intensity or DTA values.

### In Vivo Erlotinib Treatment Studies

Parent erlotinib (LC Laboratories, Woburn, MA) was resuspended in vehicle (0.3% w/v sodium carboxymethylcellulose +0.1% v/v Tween 20) and administered at 100 mg/kg *qd* via oral gavage to $n = 6$ mice until tumors regressed to roughly half their starting volume or toxicity was observed.[37−40] Control mice (vehicle-only [$n = 3$] or no administration [$n = 3$]) were treated accordingly until the tumors doubled in volume (∼600 $mm^3$). Tumor volume was defined as [$width^2$ x length]/2. Mouse weights were recorded daily, and any visible signs of toxicity were noted. Twenty-four hours following the last erlotinib administration, iPAI agents (2.5 mg/kg of both $OF650_{Erl(T)}$ and $OF550_{Erl(UnT)}$) were coadministered systemically via the tail vein. To serve as an additional control, one mouse per treatment cohort was not administered the iPAI agent. Tumors were resected 4 h following iPAI agent administration, and the tissue was fresh-frozen immediately into the OCT compound. All imaging was performed *ex vivo* after tumor resection and tissue sectioning onto glass slides as described below.

### TRIPODD: iPAI + Ab Panel Staining and Imaging

Frozen tissue blocks were sectioned at a thickness of 10 $\mu$m (Leica Biosystems cryostat, Wetzlar, Germany) onto SuperFrost Plus glass slides (ThermoFisher Scientific). To acquire full tissue iPAI fluorescence images, unmounted slides were imaged on the Zeiss AxioScan.Z1 slide scanner microscope equipped with a Colibri 7 light source (Carl Zeiss AG) and Orca Flash4 v.2 (Hamamatsu Photonics, Hamamatsu, Shizuoka, Japan). Images were collected with a 20x-0.8 M27 PlanApo objective using the following exposure times and excitation (x) and emission (m) filter combinations for image collection: OF550 at 300 ms, 550/25x, 605/70m; and OF650 at 500 ms, 640/30x, 690/50m. Following iPAI imaging, tissue sections were fixed in 4% PFA for 10 min at room temperature (RT) and stained with an antibody (Ab) viability and EGFR status panel using standard immunofluorescence protocols. Briefly, slides were washed thrice in PBS for 5 min, followed by trypsinization with 0.3% Triton-X-100/PBS for 10 min at RT. Antibodies were introduced in two stages. First, upon an additional PBS wash step (3 × 5 min), the tissue was incubated with phospho-EGFR mAb (Tyr1068, D7A5, Cell Signaling Technology) for 1 h at RT. This was followed by one wash with PBS containing Tween 20 detergent PBS-T (1 × 5 min) and two washes with PBS (2 × 5 min). The tissue was then stained with donkey antirabbit secondary + Alexa Fluor 546 (AF546, Thermo Fisher Scientific) for 45 min at RT. Subsequent PBS-T (1 × 5 min) and PBS (2 × 5 min) washes preceded additional staining with a three Ab panel consisting of the following directly conjugated mAbs for 1 h at RT: cleaved caspase 3 (CC3, Asp175) + Alexa Fluor 488 (AF488, Cell Signaling Technology), Ki67 (D3B5) + Alexa Fluor 647


https://doi.org/10.1021/acs.molpharmaceut.5c01220
Mol. Pharmaceutics 2026, 23, 1572−1585

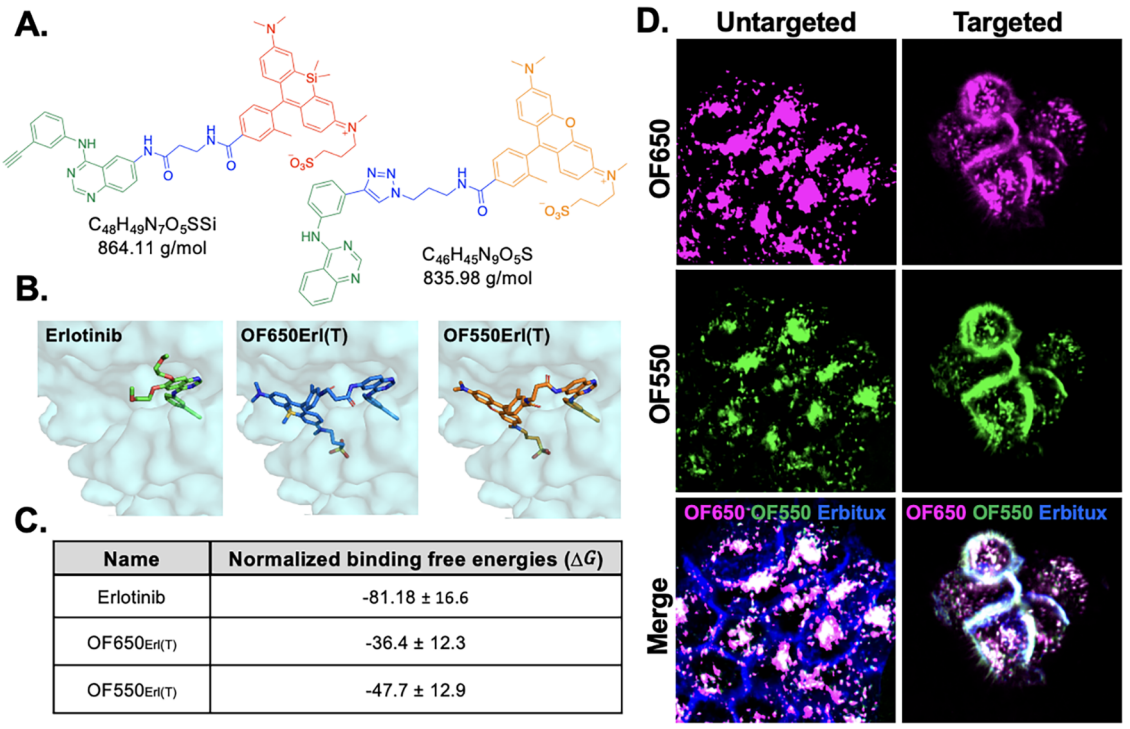


| Name | Normalized binding free energies ($\Delta G$) |
|---|---|
| Erlotinib | -81.18 ± 16.6 |
| $OF650_{Erl(T)}$ | -36.4 ± 12.3 |
| $OF550_{Erl(T)}$ | -47.7 ± 12.9 |

**Figure 1.** In silico and in vitro imaging validation of iPAI probe design. Erlotinib was fluorescently labeled with OregonFluor 650 (OF650) and OF550 to generate (A) a targeted (left) and untargeted (right) iPAI probe, respectively. (B) In silico molecular docking studies assessing the binding mode of $OF650_{Erl(T)}$ and $OF550_{Erl(UnT)}$ to epidermal growth factor receptor (EGFR) in comparison to unlabeled parent erlotinib. (C) Binding free energies for erlotinib, $OF650_{Erl(T)}$, and $OF550_{Erl(UnT)}$. (D) In vitro imaging of HCC827 cells costained with either both targeted iPAI probes ($OF650_{Erl(T)}$ and $OF550_{Erl(T)}$) or both untargeted iPAI probes ($OF650_{Erl(UnT)}$ and $OF550_{Erl(UnT)}$) and an extracellular domain EGFR antibody. OF650 images are false-colored magenta, OF550 images are false-colored green, and EGFR immunofluorescence images are false-colored blue.

(AF647, Cell Signaling Technology), and Cetuximab + Cy7 (Eli Lilly & Company, Indianapolis, IN; Lumiprobe, Hunt Valley, MD). Tissues were washed in PBS and postfixed with 4% PFA for 10 min at RT, prior to DAPI staining for nuclear visualization (Sigma-Aldrich, St. Louis, MI) and mounting with Fluoromount-G (SouthernBiotech, Birmingham, AL). Full tissue Ab panel fluorescence images were acquired on the AxioScan.Z1 using the following imaging conditions: UV (DAPI) at 5 ms, 392.5/12.5x, 445/35m; AF488 (CC3) at 600 ms, 470/40x, 525/50m; AF555 (pEGFR) at 1000 ms, 550/25x, 605/70m; AF647 (Ki67) at 200 ms, 640/30x, 690/50m; and Cy7 (EGFR) at 1000 ms, 710/75x, 810/90m. Tumor area and viability were further assessed with standard histology by hematoxylin and eosin (H&E) staining. For all whole-slide imaging, image tiles were captured with 10% overlap and stitched together using Zeiss Zen software to produce a single tissue map.

## TRIPODD Image Analysis

After iPAI and immunofluorescence image data were collected from each tissue section, the image data sets were spatially registered. The targeted and untargeted iPAI agent images were utilized to generate DTA tissue maps for each section, as described in eq 4. Targeted, untargeted, and DTA images were then manually registered to their corresponding EGFR immunofluorescence images, which served as fiducial markers for image registration of the iPAI and immunofluorescence data sets. Registration of the iPAI and immunofluorescence image data was performed with the built-in ImageJ registration plugin, "Align image by line ROI." Cell segmentation and feature extraction of the fully registered data sets were performed with QiTissue software (QiBiotech Inc., Raleigh, NC). The features that were extracted included nuclear size and mean intensity for each marker. Nuclear size was used for outlier filtering, where cells smaller than the fifth and larger than the 95th quantile of nuclear size were excluded from further analysis.

To equivalently scale the single-cell feature data from the segmented cells, the values for each protein marker, targeted iPAI agent ($OF650_{Erl(T)}$) image, untargeted iPAI agent ($OF550_{Erl(UnT)}$) image, and DTA image were z-scored using the median and standard deviation across all cells from untreated tissues for each marker. Unsupervised clustering utilizing Euclidean distance was applied to assess the potential for administration of vehicle-only treatment or iPAI injection to influence protein expression compared to the no-treatment administration and no iPAI probe injection groups, respectively. Unsupervised clustering was applied to all cells from all samples, with no knowledge of the cohort applied to the clustering algorithm. K-means clustering ($k = 5$) was applied to all cells from all samples that received iPAI injection to identify signatures of therapeutic response or no response. The $k = 5$ selection was made empirically after evaluating clustering outcomes across a range of values ($k = 2–7$). Lower values (e.g., $k = 2–3$) resulted in overly coarse separation that primarily reflected treatment versus control status without capturing within-group heterogeneity, whereas higher values ($k > 5$) produced oversegmentation and unstable, biologically redundant clusters. Cluster stability was assessed qualitatively by comparing cluster composition across independent replicates.


https://doi.org/10.1021/acs.molpharmaceut.5c01220
Mol. Pharmaceutics 2026, 23, 1572−1585

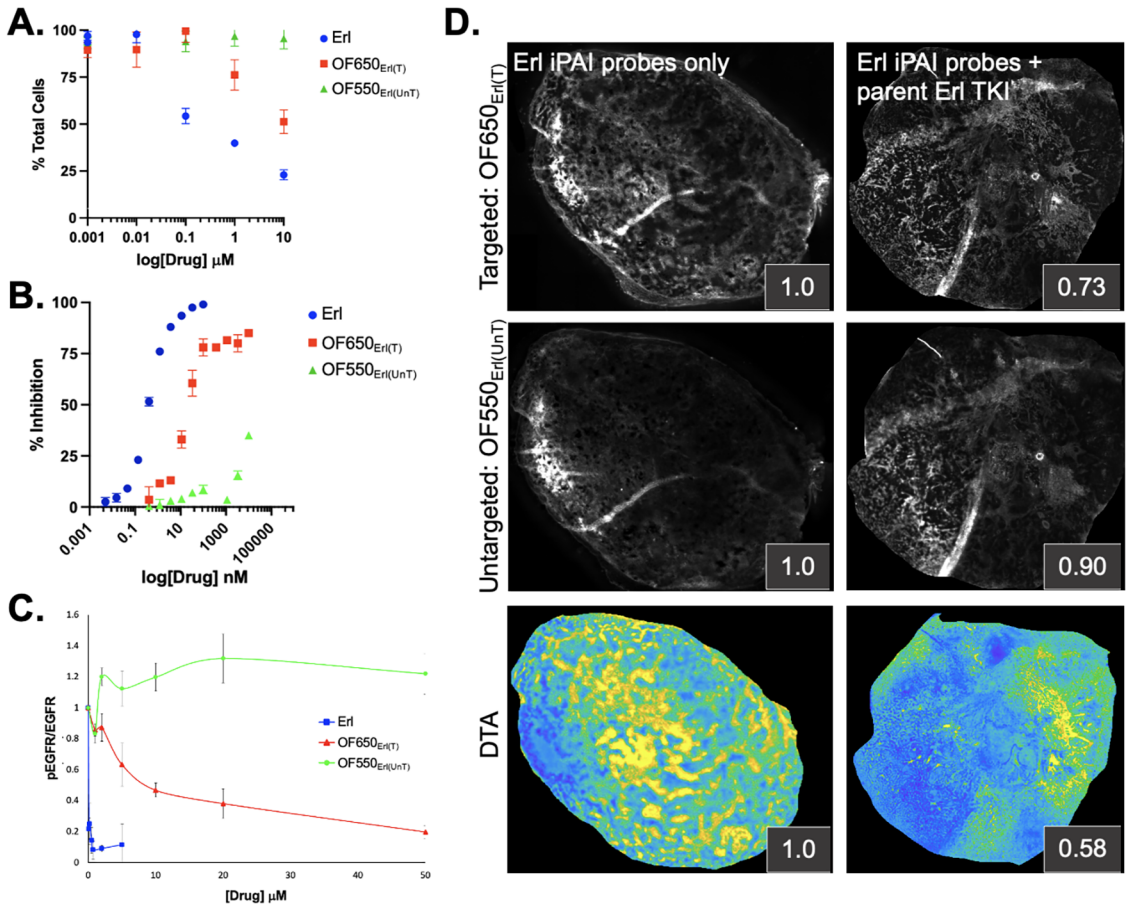


**Figure 2.** iPAI probes exhibiting targeted and untargeted behavior. (A). MTS assay of unlabeled erlotinib (Erl), $OF650_{Erl(T)}$, and $OF550_{Erl(UnT)}$ performed with HCC827 to establish $IC_{50}$ values. (B) Kinase binding assay characterized the binding affinity of Erl, $OF650_{Erl(T)}$, and $OF550_{Erl(UnT)}$ to the EGFR kinase. (C) In-cell western assay comparing the ability of Erl, $OF650_{Erl(T)}$, and $OF550_{Erl(UnT)}$ to inhibit pEGFR expression performed and reported as the pEGFR-to-EGFR immunofluorescence ratio. (D) Comparison of $OF650_{Erl(T)}$ (top row) and $OF550_{550(UnT)}$ (middle row) iPAI probe uptake performed by imaging tissue sections following administration of either iPAI probe only (left column) or tissue with iPAI probes in combination with parent erlotinib (right column), where images are displayed with autocontrast. DTA tissue maps (bottom row) were calculated and are scaled to be equivalent. Relative signal intensities comparing each injection condition per imaging channel are presented as inset values.

## RESULTS

### In Silico Molecular Dynamics of Erlotinib and iPAI Probe Binding

Molecular dynamics (MD) simulations were performed to evaluate the targeted agent (T) and untargeted agent (UnT) binding behavior of the erlotinib iPAI agents (Figure 1A) into the EGFR ATP-binding pocket compared with the binding of the erlotinib parent drug. The four agent configurations that were simulated included (1) $OF650_{Erl(T)}$, (2) $OF650_{Erl(UnT)}$, (3) $OF550_{Erl(T)}$, and (4) $OF550_{Erl(UnT)}$. The iPAI-targeted agents ($OF650_{Erl(T)}$ and $OF550_{Erl(T)}$) demonstrated binding modes similar to the parent erlotinib drug-binding mode (Figure 1B). Binding free energies ($\Delta G$) were calculated for EGFR bound to the parent erlotinib drug, $OF650_{Erl(T)}$, and $OF550_{Erl(T)}$ (Figure 1C). Normalized $\Delta G$ for EGFR bound to parent erlotinib was −81.84 kJ/mol and −36.44 kJ/mol for EGFR bound to $OF650_{Erl(T)}$ and −47.71 kJ/mol for EGFR bound to $OF550_{Erl(T)}$. The molecular dynamics of binding between the iPAI-untargeted agents ($OF650_{Erl(UnT)}$ and $OF550_{Erl(UnT)}$) and EGFR was also assessed. However, after minimization, $OF650_{Erl(UnT)}$ completely dissolved from EGFR, while $OF550_{Erl(UnT)}$ stayed intact but was pulled out from the EGFR-binding pocket, showing their untargeted behavior (Figure S1A,B). Since the control agents did not bind to EGFR, the binding free energies could not be reliably calculated.

### In Vitro iPAI Agent Binding and Targeted Activity Characterization

Targeted and untargeted behavior of erlotinib iPAI agents was evaluated in vitro by costaining cells with the iPAI agents and EGFR immunofluorescence to compare iPAI agent cellular localization to that of the EGFR protein. The untargeted iPAI agents ($OF550_{Erl(UnT)}$ and $OF650_{Erl(UnT)}$) demonstrated diffuse intracellular localization within the cytoplasm (Figure 1D). Overlaid images of the untargeted iPAI agents and EGFR immunofluorescence showed that both untargeted iPAI agents had similar cytoplasmic localization, while EGFR localized to the cell membrane showed minimal colocalization of the EGFR protein with either of the untargeted iPAI agents. The targeted iPAI agents ($OF550_{Erl(T)}$ and $OF650_{Erl(T)}$) were observed to primarily stain cell membranes, with some intracellular, cytoplasmic localization observed. Overlays of the targeted iPAI agents and EGFR immunofluorescence images demonstrated colocalization of membrane-specific signals, while the intracellular signal from the targeted iPAI agents showed minimal colocalization with EGFR antibody


https://doi.org/10.1021/acs.molpharmaceut.5c01220
Mol. Pharmaceutics 2026, 23, 1572−1585

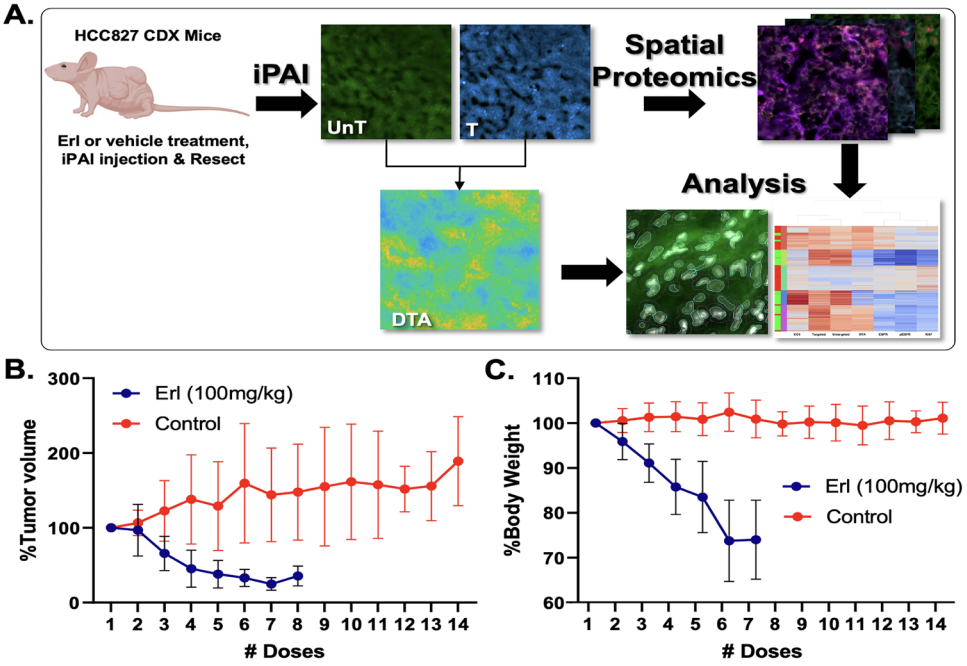


**Figure 3.** TRIPODD analysis of erlotinib-treated HCC827 CDX mice. (A) HCC827 mice were treated with either erlotinib ($n$ = 6), vehicle ($n$ = 3), or left untreated ($n$ = 3) followed by iPAI probe injection prior to euthanasia, tumor resection, tissue processing, and downstream TRIPODD analysis. (B) Tumor volume and (C) body weight change measured following each Erl dose to assess therapeutic efficacy and toxicity.

staining (Figure 1D). Notably, both colors (i.e., OF550 and OF650) of the targeted and untargeted iPAI agents exhibited highly colocalized in vitro staining patterns, permitting selection of a single pair for additional characterization, where the $OF650_{Erl(T)}$ and $OF550_{Erl(UnT)}$ iPAI pair were used in subsequent studies.

Targeted activity was further characterized by quantifying therapeutic efficacy and binding affinity, as quantified using percent inhibition and pEGFR/EGFR ratios of the selected iPAI-targeted and untargeted pair, $OF650_{Erl(T)}$ and $OF550_{Erl(UnT)}$, compared to the unlabeled parent erlotinib. Therapeutic efficacy was quantified in the erlotinib-sensitive HCC827 cells. The untargeted iPAI agent, $OF550_{Erl(UnT)}$, showed minimal effect on cell proliferation at doses ranging from 0 to 10 $\mu$M. The targeted iPAI agent, $OF650_{Erl(T)}$, demonstrated dose-dependent proliferation inhibition in HCC827 cells but exhibited lower therapeutic efficacy than unlabeled, parent erlotinib (Figure 2A). Percent inhibition quantification showed that parent erlotinib exhibited dose-dependent kinase binding and superior affinity to either the targeted or untargeted iPAI agents. The targeted iPAI agent exhibited a greater kinase binding affinity than the untargeted iPAI agent, which showed a minimal kinase binding affinity (Figure 2B). Binding efficiency was also quantified as the ratio of pEGFR to EGFR expression measured by immunofluorescence for cells treated with either parent erlotinib, $OF650_{Erl(T)}$, or $OF550_{Erl(UnT)}$. Parent erlotinib showed substantially greater binding efficiency than either iPAI agent, where low pEGFR/EGFR ratios were observed with doses >10 $\mu$M of the parent erlotinib. Similar to other validation assays, $OF650_{Erl(T)}$ showed a greater binding efficiency than $OF550_{Erl(UnT)}$. Cells dosed with $OF650_{Erl(T)}$ showed pEGFR/EGFR ratios that decreased with increasing dose. However, for cells treated with $OF550_{Erl(UnT)}$, there was no observable dose-dependent relationship between pEGFR/EGFR ratios and administered dose. further validating the targeted and untargeted behavior of each iPAI agent (Figure 2C).

## In Vivo Competitive Binding of iPAI Agents and Erlotinib Parent Drug

Competition for the erlotinib EGFR-binding site was assessed for the targeted iPAI agent and parent erlotinib via in vivo administration in tumor-bearing mice. HCC827 xenograft-bearing mice were administered either the erlotinib iPAI agent pair only or the erlotinib iPAI probe pair plus the parent erlotinib TKI. Targeted and untargeted iPAI agent intensities were measured on whole-tissue section images, enabling the quantification of relative fluorescence intensities and calculation of DTA for each representative image (Figure 2D). The relative targeted iPAI agent intensity was highest in the HCC827 tissue following erlotinib iPAI agent administration without parent erlotinib. The HCC827 tissue that received both the erlotinib iPAI agents and erlotinib parent TKI exhibited a 27% lower relative targeted iPAI agent intensity. In contrast, the relative untargeted iPAI agent signal was only 10% lower in the HCC827 tissue that received both the erlotinib iPAI agents and parent erlotinib compared to the HCC827 tissue that received only the iPAI agents. DTA tissue maps were calculated for each tissue section and scaled equivalently by applying the same contrast settings to both DTA tissue maps. Calculated relative DTA showed a 42% increase in the tissue that received the erlotinib iPAI agents only vs coadministration of the agents with parent erlotinib, demonstrating that the targeted iPAI agent competes for the same EGFR-binding sites as the parent erlotinib. Comparing the relative targeted iPAI probe intensities alone (i.e., 73%) to the binding difference by DTA (i.e., 58%) suggests that there is ~15% more bound parent erlotinib when measured by DTA compared to when measured by targeted iPAI probe intensity alone. This suggests that nonspecific accumulation of the targeted iPAI probe can skew results and cause under-


https://doi.org/10.1021/acs.molpharmaceut.5c01220
Mol. Pharmaceutics 2026, 23, 1572−1585

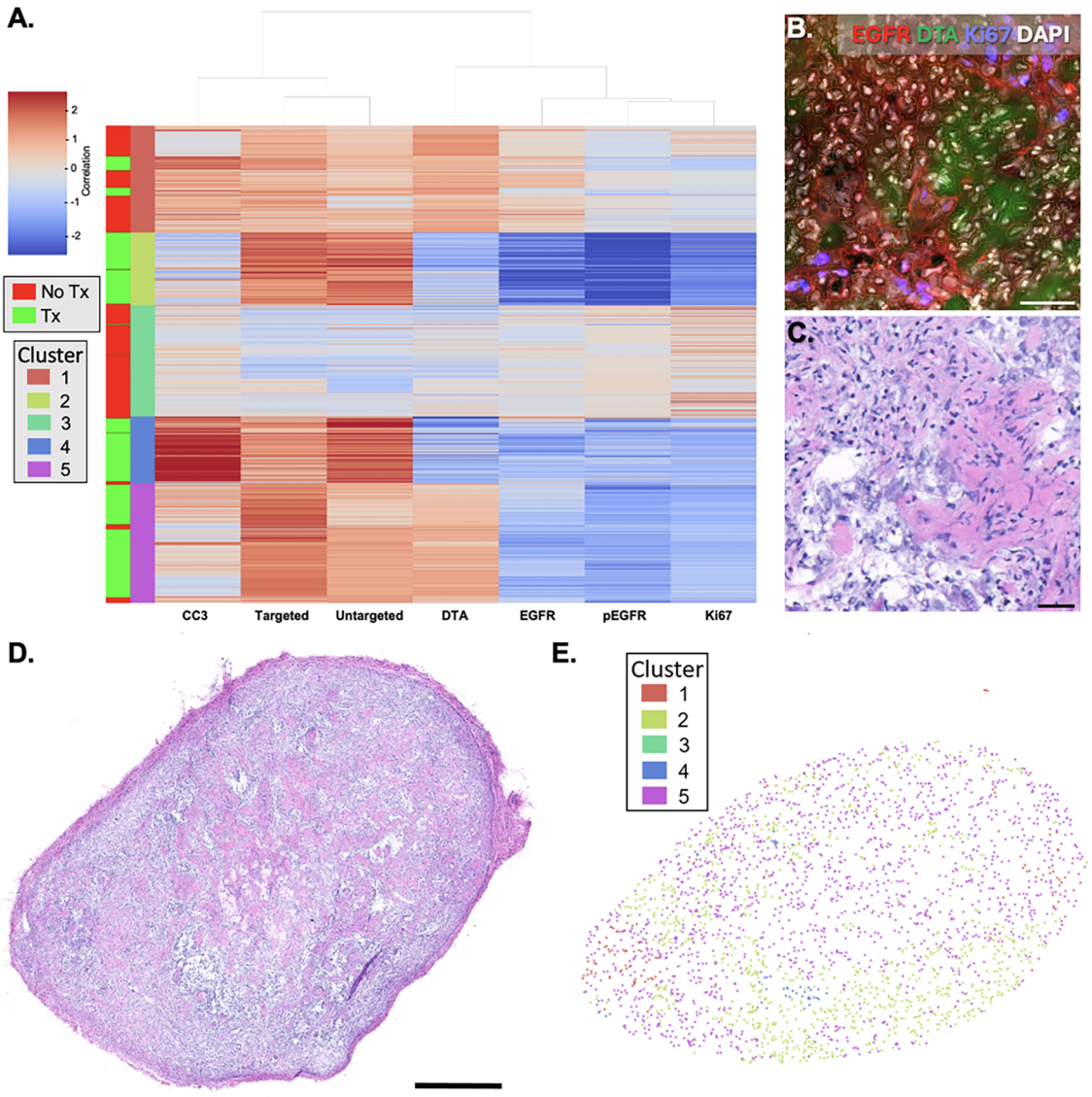


**Figure 4.** TRIPODD characterization of unique signatures of therapeutic response. (A) K-means clustering was applied to single-cell feature imaging data (from $n = 6$ erlotinib-treated, $n = 6$ vehicle control mice) to characterize signatures of therapeutic response based on proteomic, DTA, and iPAI signals and identify unique cell populations. (B) Representative region of interest (ROI, scale bar = 50 $\mu$m) from a treated tissue displaying the spatial context of EGFR, DTA, and Ki67 expression, where (C) tissue viability was shown using standard H&E staining (scale bar = 50 $\mu$m). (D) Full tissue image of H&E staining of the same tissue revealing the shape of the tissue section (scale bar = 500 $\mu$m) to give context to the (E) mixture of cell cluster identities shown in the scatter plot of cell locations, which were color-coded by K-means cluster identity.

estimation of the targeted bound drug, in this case, erlotinib (Figure 2B).

## Erlotinib Treatment of HCC827 CDX Mice

After HCC827 xenografts reached ~300 mm$^3$, mice were randomly selected for placement into one of the following cohorts: (1) 100 mg/kg erlotinib treatment, (2) vehicle-only, or (3) no treatment ($n = 4$ mice per group). Once tumors doubled in volume (600 mm$^3$) or shrank to 100 mm$^3$, mice were euthanized, tumors were resected, and the tissue was processed for TRIPODD analysis (Figure 3A). The treated cohort demonstrated sensitivity to erlotinib, as evidenced by a rapid decrease in tumor volume, while the control mice displayed a notable increase in tumor volume (Figure 3B). Bodyweight also decreased in the erlotinib-treated cohort compared with the control mice whose body weight remained stable (Figure 3C). Similar trends in tumor volume growth and body weight change were observed between the two control cohorts (Figure S2).

All tissues were processed by using the TRIPODD analysis platform. Following spatial registration, cell segmentation, and processing of iPAI and immunofluorescence imaging data, unsupervised clustering of the cells revealed that there was minimal difference in protein expression between the vehicle-treated and no-treatment populations within the control cohorts. Therefore, samples from the vehicle-treated and no-treatment groups were considered as a single control cohort in downstream analyses (Figure S3A). Unsupervised clustering comparing mice injected with iPAI agents and mice not injected with iPAI agents further revealed that the single iPAI dose had minimal effect on protein expression (Figure S3B).

K-means clustering of single-cell feature data revealed five distinguishable cell populations (Figure 4A). Clusters 1 and 3 were largely composed of cells from the control group and


https://doi.org/10.1021/acs.molpharmaceut.5c01220
Mol. Pharmaceutics 2026, 23, 1572−1585

shared similar EGFR, pEGFR, and Ki67 levels as markers of cell viability. The major observed differences between clusters 1 and 3 were the increased levels of cleaved caspase 3 (CC3), targeted and untargeted iPAI agent signals, and DTA. Cells from tissues treated with 100 mg/kg erlotinib were separated into three distinct clusters (i.e., clusters 2, 4, and 5). Cluster 2, 4, and 5 were all composed of cells with decreased cell viability proteomic signatures (i.e., EGFR, pEGFR, and Ki67) relative to the median value of control tissues. Clusters 2, 4, and 5 also all exhibited targeted and untargeted iPAI agent levels greater than the median value of vehicle-treated cells. Cluster 2 was composed of cells largely with CC3 expression near the median level in vehicle-treated cells and DTA below the median value of vehicle-treated cells. Cluster 4 contained cells with a high expression of CC3, relative to the median levels of vehicle-treated cells, indicative of cells undergoing apoptosis. Additionally, cells in cluster 4 generally exhibited DTA values below the median DTA of cells from the control cohort. Cluster 5 showed a similar distribution of CC3 to cluster 2, but the cells largely exhibited DTA values higher than the median DTA from control tissue cells.

Visualization of DTA and EGFR spatial patterns in a representative region of interest from a treated tissue demonstrated lower DTA within the tumor cells (EGFR+) relative to the nontumor tissue areas (EGFR−, Figure 4B). This spatial pattern observation aligns with the fact that systemically administered iPAI agents were delivered to the xenograft tumor cells through the nontumor, mouse vasculature. In these nontumor areas, DTA would be higher, as few drug targets would be expressed and minimal drug would bind. Additionally, while there were many tumor cells present, as delineated by the EGFR+ signal, there were a few proliferating cells, consistent with the K-means clustering results. Furthermore, H&E staining revealed a loss of tumor cell organization and a decrease in the overall population of viable tumor cells (Figure 4C). In contrast, a representative image from a control tissue showed a greater proportion of Ki67+ tumor cells (Figure S4A) and a more organized, viable tumor sample (Figure S4B). A scatter plot of cell locations within a treated sample, with each cell color-coded by cluster identity, revealed a mixture of clusters within a single sample (Figure 4D,E). As shown by the overall K-means cluster results, the three main clusters present in the treated sample were clusters 2, 4, and 5, which were all largely composed of cells from treated samples. A similar scatter plot of cell locations from a representative control sample revealed a mixture of clusters 1 and 3, which were composed of untreated cells (Figure S4C). In both representative spatial plots of the clustering results, distinct regions of tissue were also identified, where cells from the same cluster were predominantely located together, suggesting that features of the tumor and its TME drive proteomic expression, iPAI agent distribution, and DTA levels.

Signal intensity of all markers was also visually assessed in representative ROIs from the control, no-treatment cohort, and the treated cohort (Figure 5). Height maps of DTA signals permitted three-dimensional (3D) visualization of DTA intensity, where the height per pixel represented the quantified level of DTA at that pixel. Height maps in all images were scaled equivalently across the control and treated images for qualitative comparison (Figure 5A,5B). Additionally, the contrast level of each immunostained biomarker and DTA was set equivalently across all images from both cohorts to enable qualitative assessment. DTA height maps between the treated and control images revealed differences in the pattern of DTA distribution and in the level of DTA present in each cohort. In the control tissue, DTA height map topography and pixel pseudo-color intensity were relatively consistent across

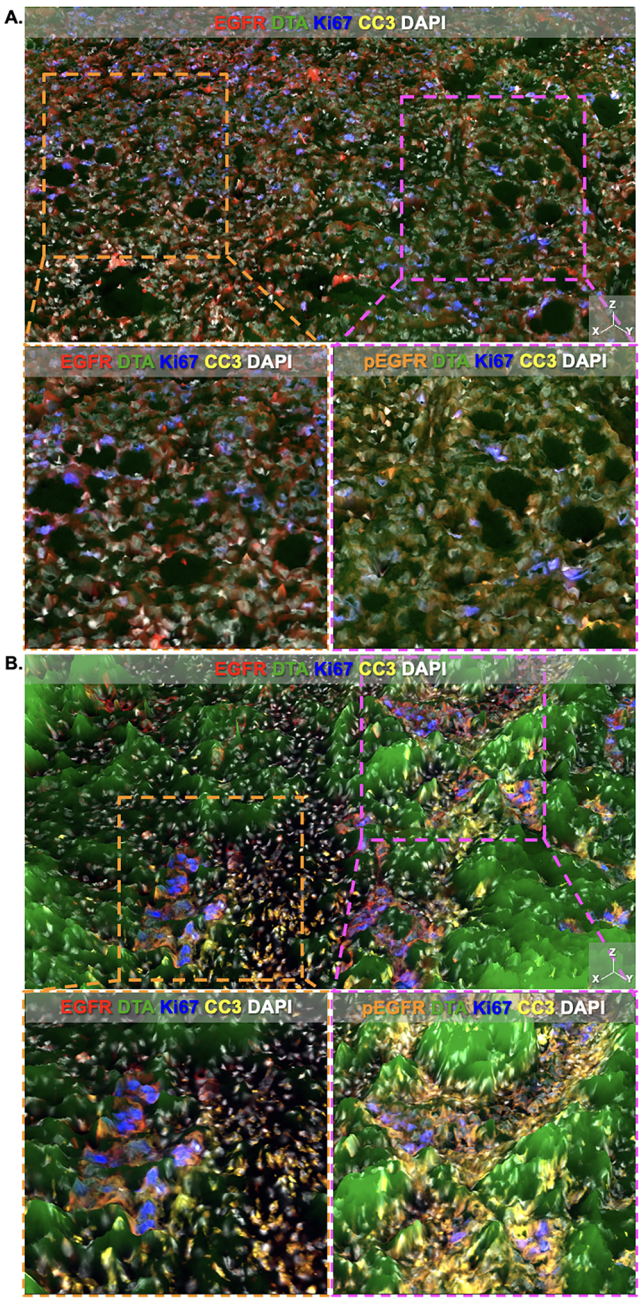


**Figure 5.** 3D visualization of DTA and protein markers of viability in control and treated tissue samples. Representative regions of interest (ROIs) from whole-tissue images of HCC827 xenografts imaged using multiplexed immunofluorescence and iPAI shown for (A) a control, no-treatment (No Tx) xenograft tissue sample and (B) a treated (Tx) xenograft tissue sample. In each image, the DTA signal is represented as a 3D height map, where DTA can be visualized both by its green pseudo-color and pixel height. DTA height map scaling was applied equivalently in all displayed images. For each panel, the images shown below the overview image represent the ROIs outlined by the orange or pink boxes in the 3D images to visualize all proteomic markers. The proteomic markers displayed in each image are displayed equivalent contrast settings across treatment groups.


https://doi.org/10.1021/acs.molpharmaceut.5c01220
Mol. Pharmaceutics 2026, 23, 1572−1585

the image (Figure 5A). Additionally, in the control tissue, expression of EGFR (Figure 5A, orange box) and pEGFR (Figure 5A, pink box) were consistent across the images. Cell proliferation, as visualized by Ki67 expression, was homogeneous across the control tissue ROI, while cell apoptosis, as visualized by CC3, was not readily observed in this representative ROI. In contrast to the control tissue, the DTA map for the treated sample showed substantially more heterogeneity in the DTA height map topography and pixel intensity (Figure 5B). Furthermore, positive EGFR (Figure 5B, orange box) and pEGFR (Figure 5B, pink box) signals were present but were more heterogeneous than in the control sample. Additionally, in the treated sample, Ki67 expression appeared more limited, while CC3 expression was readily visible. Notably, these qualitative observations on the ROIs of representative images were in alignment with the quantified results (Figures 4 and S4).

## DISCUSSION

Accurate quantification of drug localization within the TME is paramount to understanding and predicting therapeutic outcomes for patients. Many molecularly targeted therapeutics bind to intracellular targets, which are not readily accessible in live cells due to the plasma membranes. Furthermore, current drug engagement measurements are largely limited to bulk sampling (e.g., plasma analysis) and indirect measurements of therapeutic response (e.g., western blotting). Efficiently modifying standard-of-care therapeutics with fluorescent readouts provides a unique opportunity to probe high-affinity, small-molecule targeted drugs with direct relevance to the clinic. As such, cell membrane-permeant, fluorescently labeled small molecules targeting intracellular domains afford the unique opportunity to probe the intracellular proteome and quantify therapeutic efficacy.[13] Herein, fluorescently labeled erlotinib probes were utilized to quantitatively evaluate DTA of the EGFR kinase signaling cascade, an attractive therapeutic target, owing to the aberrant nature of this pathway in many diseases. The TRIPODD platform provides an opportunity to fill an unmet need by combining spatially resolved iPAI and cyclic immunofluorescence on a single tissue.[8,9]

The validation of targeted and untargeted iPAI agent activity, as well as extension of the TRIPODD platform to assess longitudinal therapeutic response, was evaluated. The on-target binding activity of two targeted and two untargeted (control) erlotinib iPAI agents—$OF650_{Erl(T)}$, $OF550_{Erl(T)}$, $OF650_{Erl(UnT)}$, and $OF550_{Erl(UnT)}$—to the EGFR ATP-binding pocket was assessed using in silico molecular docking studies. Both targeted agents, $OF650_{Erl(T)}$ and $OF550_{Erl(T)}$, displayed EGFR binding modes similar to those the parent erlotinib drug, demonstrating their affinity for the EGFR target (Figure 1B). Validation of the untargeted agents, $OF650_{Erl(UnT)}$ and $OF550_{Erl(UnT)}$, was also demonstrated, as neither agent bound appreciably to the EGFR ATP-binding pocket (Figure S1A,B). Binding free energy ($\Delta G$) calculations of all iPAI agent configurations confirmed that both targeted agents retain EGFR-binding affinity, while the $\Delta G$ could not be calculated for either untargeted agent since neither successfully bound to the EGFR ATP-binding pocket (Figures 1C and S1). Root-mean-square fluctuation (RMSF) of parent erlotinib and all iPAI probe configurations confirmed that all erlotinib iPAI agent configurations facilitated some conformational changes in EGFR around the protein residues 845−852 (Figure S1C,D).

Further iPAI probe validation was assessed in vitro by costaining HCC827 cells with an EGFR extracellular domain-targeted antibody and either the targeted iPAI probes, $OF650_{Erl(T)}$ and $OF550_{Erl(T)}$, or the untargeted iPAI probes, $OF650_{Erl(UnT)}$ and $OF550_{Erl(UnT)}$ (Figure 1D). Minimal colocalization with the cell membrane-specific staining pattern of the EGRF antibody was observed for both untargeted agent configurations (i.e., $OF650_{Erl(UnT)}$ and $OF550_{Erl(UnT)}$), demonstrating their untargeted activity and reduced EGFR-binding affinity. In contrast, substantial cell membrane-specific staining patterns, colocalized with the EGFR antibody, were observed for the targeted agent configurations (i.e., $OF650_{Erl(T)}$ and $OF550_{Erl(T)}$). Additionally, no major difference in the staining pattern was observed between the two targeted agent configurations. Observed colocalization between the targeted probes and the EGFR antibody provided in vitro validation of the on-target activity of the targeted iPAI agents. Considering this in vitro result along with the in silico molecular docking studies, the optimal iPAI agent pair configuration was determined to be $OF650_{Erl(T)}$ and $OF550_{Erl(UnT)}$ for subsequent studies utilizing iPAI agents.

Therapeutic efficacy of the optimal iPAI agent pair, $OF650_{Erl(T)}$ and $OF550_{Erl(UnT)}$, was assessed to determine the extent to which therapeutic efficacy was perturbed after erlotinib fluorophore modification. The half-maximal inhibitory concentration ($IC_{50}$) values for unlabeled, parent erlotinib, and $OF650_{Erl(T)}$ and $OF550_{Erl(UnT)}$ were quantified (Figure 2A). Parent erlotinib demonstrated the greatest $IC_{50}$ concentration value, 0.27 nM, followed by $OF650_{Erl(T)}$, 8.62 nM. Notably, the $IC_{50}$ value of $OF550_{Erl(UnT)}$ could not be calculated, as no concentration of $OF550_{Erl(UnT)}$ demonstrated an observable in vitro inhibitory effect. Notably, the targeted agent, $OF650_{Erl(T)}$, demonstrated proliferation inhibitory activity ($IC_{50}$ = 8.62 $\mu$M), albeit with reduced efficacy compared to the parent erlotinib ($IC_{50}$ = 0.27 $\mu$M). A similar result was also observed in a kinase binding assay comparing parent erlotinib with $OF650_{Erl(T)}$ and $OF550_{Erl(UnT)}$ for EGFR kinase binding affinity in vitro (Figure 2B). Kinase binding affinity, measured by percentage kinase inhibition, demonstrated that $OF550_{Erl(UnT)}$ had the lowest kinase binding affinity of 3.73 $\mu$M, while $OF650_{Erl(T)}$ exhibited substantially greater kinase binding affinity of 16.84 nM, although this remained lower than that of parent erlotinib, which demonstrated a kinase binding affinity of 0.40 nM. The binding free energy of $OF650_{Erl(T)}$ was ∼55% lower than that of parent erlotinib, indicating that $OF650_{Erl(T)}$ had lower binding affinity for the EGFR ATP-binding pocket and therefore lower efficacy than parent erlotinib. Together, these in vitro binding studies confirmed the targeted iPAI agent reliably maintained binding affinity to EGFR as a robust readout for erlotinib localization, while the untargeted, the control iPAI agent had the expected disrupted binding affinity to mimic nonspecific therapeutic binding.

In vivo validation of targeted and untargeted iPAI agent activity was quantified through a competitive binding study in xenografted tumor tissue (Figure 2D). There was a greater relative decrease in fluorescence signal intensity in the targeted agent imaging channel compared to the untargeted agent imaging channel in the tissues when the iPAI probes were coadministered with parent erlotinib (i.e., competitive binding tissues). This suggested that the targeted agent competed with parent erlotinib for the EGFR ATP-binding sites. Furthermore, the calculated relative DTA in the competitive binding tissue


https://doi.org/10.1021/acs.molpharmaceut.5c01220
Mol. Pharmaceutics 2026, 23, 1572−1585

was 42% lower than that of tissues that received only the iPAI agents without the parent erlotinib. This data, in conjunction with our previously reported studies,[8,9,13] demonstrated the potential of the DTA metric to detect the presence of parent erlotinib and therefore the potential for the TRIPODD platform to characterize drug-binding spatial distribution during the treatment course.

As a proof-of-principle to assess therapeutic response using the TRIPPODD platform, HCC827 xenograft-bearing mice were divided into either control or erlotinib treatment cohorts, where iPAI agents were injected just prior to euthanasia. Unsupervised cluster analysis revealed that iPAI injection had minimal influence on biomarker expression (Supporting Figure 2A). Following tumor tissue resection, image collection (i.e., iPAI and immunofluorescence imaging), and downstream analysis, most control cohort cells retained similar "cell viability" biomarker expression, defined herein as EGFR, pEGFR, and Ki67 (Figure 4A). However, the control tissue cells displayed variability in cleaved caspase 3 (CC3), targeted and untargeted iPAI agent uptake, and DTA, which resulted in statistical separation of clusters 1 and 3. This observation was additionally evident through the spatial distribution of iPAI agents. Therefore, the heterogeneous erlotinib parent drug distribution in untreated xenograft tissues may be due to key features of tissue architecture, such as vasculature and lymphatics, for transport.

The iPAI signatures of the treated cells fluctuated across three unique clusters, demonstrating the variability of drug delivery and subsequent distribution across tissues. Notably, DTA was decreased in the presence of parent erlotinib, indicating an inverse relationship between DTA and the presence of parent erlotinib. However, a comparison of the full TRIPODD signature (i.e., iPAI + immunofluorescence single-cell intensities) suggested that cluster 4 was composed mostly of apoptotic cells (CC3-positive), demonstrating that DTA alone was insufficient to characterize the therapeutic effect. A comparison of the nonapoptotic TRIPODD signatures observed in clusters 2 and 5 revealed similar cell viability signatures, while EGFR, pEGFR, and Ki67 were quantified at subcontrol levels. This was in line with the measured sensitivity of HCC827 cells to erlotinib treatment. However, the major difference between clusters 2 and 5 was in their DTA levels. The TRIPODD signature in cluster 2 suggested that while exhibiting the effects of treatment with measurable erlotinib still present in the cells as measured by DTA, these cells were not yet undergoing apoptosis. Therefore, the TRIPODD signature in cluster 5 suggested that a sublethal dose of erlotinib had reached these cells, as apoptosis did not appear to be ongoing based on the CC3 levels. This sublethal dose delivery resulted in suppressed cell viability, which subsequently resulted in a more rapid clearance of the lower drug concentration from the cells, which led to elevated DTA levels. The spatial variability of DTA in treated tissues was visualized as variable DTA levels (Figure 4B). Interestingly, there were regions of high DTA in the nontumor cell regions that were identified by the lack of EGFR. Since the nontumor cell regions were mouse stromal tissue where erlotinib and iPAI agents were delivered through the mouse vasculature, spatial mapping of the various cluster identities per cell was identifiable, where a mix of clusters was observed on a single tissue section, demonstrating the potential for inter- and intratumoral variability of drug delivery (Figure 4E).

Notably, the signatures of DTA and protein expression were also visualized in representative ROIs from a control, untreated tissue sample, and a treated tissue sample (Figure 5). The 3D height map of DTA from the control sample showed baseline DTA topography (Figure 5A). In the control samples where erlotinib was not present, it was evident that DTA was roughly equivalent across the ROI with slight variations, as visualized by the DTA height map, which was supported by the clustering of untreated cells to clusters 1 and 3 (Figure 4A). Importantly, clusters 1 and 3 did not exhibit marked differences in proteomic expression. Comparison of the DTA topography in the treated tissue versus that in the control tissue showed substantially greater DTA heterogeneity in the treated samples (Figure 5B). Importantly, the areas with low DTA were largely composed of viable tumor cells, which were positive for EGFR, pEGFR, and Ki67, and dying cells, which were positive for CC3. This was indicative of bound erlotinib in these areas where the molecular target was present and likely to bind in the erlotinib-sensitive HCC827 xenografts. The surrounding areas, where DTA was elevated, showed some CC3-positive cells but mostly appeared as cells devoid of positive signal for any of the stained biomarkers, suggesting that they may have been mouse stromal tissue infiltrate or areas of dead cells that no longer expressed CC3, and erlotinib was no longer present. Notably, these qualitative observations were in alignment with the results of the performed cluster analyses. Clusters 2 and 5 were largely composed of tumor cells that had not yet undergone apoptosis, with the major difference being in the DTA levels. Inspection of the treated tissue DTA maps revealed that some areas of viable tumor were adjacent to nontumor areas with high DTA, while other viable tumor cells appeared to have lower DTA. It is unclear what factors influenced the difference in DTA between clusters 2 and 5 in the current work and will be investigated further in subsequent studies. The confirmation of the quantitative cluster analysis results and the qualitative observations in the representative ROIs provided evidence that DTA can be a spatially resolved metric for assessing a single-cell therapeutic response for the first time in a longitudinal treatment study (Table 1).

This proof-of-principle longitudinal erlotinib treatment study in HCC827 xenograft tissues demonstrated the utility of the TRIPODD platform to identify unique signatures of therapeutic response and nonresponse using the combination of iPAI and immunofluorescence signatures. The relatively small sample size was intentional for this proof-of-principle study, where future studies will require an increased sample size to evaluate the TRIPODD platform's ability to identify unique signatures of therapeutic response. The increased sample size will also enable exploration into the impact that reduced affinity by the targeted probe relative parent drug has on analysis results in cases where DTA fails to correlate with biomarker signatures. The limited immunofluorescence panel in this proof-of-principle study did not facilitate further spatial analysis of tissue architecture to assess this observation and identify key tissue architectural features (e.g., vasculature and lymphatic vessels) that may play a role in variable drug delivery. Future studies will incorporate extended immunofluorescence panels to study downstream cell signaling in the EGFR cascade, as well as the role that tissue architecture plays in the TRIPODD signatures to enhance spatial analyses of local neighborhoods of similar TRIPODD signatures and the use of more sophisticated clustering approaches, facilitating greater resolution of TRIPODD signatures.[41−43] Additionally,


https://doi.org/10.1021/acs.molpharmaceut.5c01220
Mol. Pharmaceutics 2026, 23, 1572−1585

Table 1. TRIPODD K-Means Clustering Analysis Summary[a]

| cluster | cohort | biomarker features | biological interpretation | spatial/phenotypic notes |
|---|---|---|---|---|
| 1 | control | above-median targeted and untargeted iPAI and DTA; variable apoptosis (CC3) | reflects intratumoral heterogeneity in untreated tissue; indicates regions with higher iPAI probe penetration or local drug accumulation | heterogeneous iPAI uptake, potentially driven by vascular and tissue architectural features |
| 2 | treated | subcontrol DTA; subcontrol EGFR, pEGFR, proliferation (Ki67); nonapoptotic | indicates erlotinib-engaged cells with measurable parent drug occupancy but not yet undergoing apoptosis | cells located within viable tumor areas with low DTA |
| 3 | control | median iPAI and DTA levels; variable apoptosis (CC3) | represents baseline viability and apoptosis balance within untreated xenografts | corresponds to control tissue DTA with relatively low variation |
| 4 | treated | high apoptosis (CC3); decreased DTA | primarily apoptotic cells; reflects effective erlotinib engagement leading to programmed cell death | spatially corresponds to apoptotic tumor zones visible in treated tissues |
| 5 | treated | above-control DTA levels; subcontrol EGFR/pEGFR/Ki67; low apoptosis (CC3) | suggests sublethal erlotinib exposure—reduced viability markers with rapid drug clearance and elevated residual DTA levels | -cells located within viable tumor areas, DTA levels similar to control cells in cluster 1 |

[a]DTA = drug target availability, CC3 = cleaved caspase 3, iPAI = intracellular paired agent imaging, EGFR = epidermal growth factor receptor, pEGFR = phosphorylated epidermal growth factor receptor.

the HCC827 xenograft model was employed for the development and validation of the TRIPODD platform, but future studies will incorporate immune-competent model systems to assess the role of the TME and immune infiltrate in drug delivery and efficacy. Additionally, future studies will incorporate later-generation EGFR TKIs (e.g., osimertinib), which are superior to erlotinib in effectively treating EGFR-mutated NSCLC,[44] increasing the generalizability of the TRIPODD platform. The data presented herein provide validation of the TRIPODD imaging platform's capability to characterize in situ therapeutic response and mechanisms of therapeutic resistance. The TRIPODD platform can be readily applied to a broad range of model systems, where further development of platform will enable the study of novel therapeutic strategies.

## ■ ASSOCIATED CONTENT

### Supporting Information

The Supporting Information is available free of charge at https://pubs.acs.org/doi/10.1021/acs.molpharmaceut.5c01220.

In silico molecular docking studies for the untargeted erlotinib agents, tumor growth and weight curves demonstrating that vehicle treatment did not affect either parameter, clustering results showing that neither vehicle injection nor iPAI injection affected measured protein expression, and TRIPODD platform characterization of the control tumor tissues (PDF)

## ■ AUTHOR INFORMATION


### Corresponding Author

**Summer L. Gibbs** − *Biomedical Engineering Department and Knight Cancer Institute, Oregon Health & Science University, Portland, Oregon 97201, United States;* orcid.org/0000-0001-8077-1582; Phone: 503-494-8940; Email: gibbss@ohsu.edu

### Authors

**Nathan P. McMahon** − *Biomedical Engineering Department, Oregon Health & Science University, Portland, Oregon 97201, United States*

**Allison Solanki** − *Biomedical Engineering Department, Oregon Health & Science University, Portland, Oregon 97201, United States*

**Antonio R. Montaño** − *Biomedical Engineering Department, Oregon Health & Science University, Portland, Oregon 97201, United States*

**E. Sila Ozdemir** − *Cancer Early Detection Advanced Research Center, Oregon Health & Science University, Portland, Oregon 97201, United States*

**Kimberley S. Samkoe** − *Thayer School of Engineering at Dartmouth College and Department of Surgery, Geisel School of Medicine at Dartmouth College, Dartmouth College, Hanover, New Hampshire 03755, United States;* orcid.org/0000-0002-8234-2308

**Kenneth M. Tichauer** − *Biomedical Engineering, Illinois Institute of Technology, Chicago, Illinois 60616, United States*

**Lei G. Wang** − *Biomedical Engineering Department and Knight Cancer Institute, Oregon Health & Science University, Portland, Oregon 97201, United States;* orcid.org/0000-0002-0664-2704




https://doi.org/10.1021/acs.molpharmaceut.5c01220
Mol. Pharmaceutics 2026, 23, 1572−1585

Complete contact information is available at:
https://pubs.acs.org/10.1021/acs.molpharmaceut.5c01220

### Author Contributions

[▽]N.P.M. and A.S. contributed equally to this work.

### Notes

The authors declare the following competing financial interest(s): L.G.W., A.R.M. and S.L.G. are inventors on patent application PCT/US21/53806, Zwitterionic cell-permeant and water-soluble rhodamine dyes for quantitative imaging applications, submitted to the World Intellectual Property Organization and held by Oregon Health and Science University that covers the composition and methods of use of the ORFluor compounds used herein.

## ■ ACKNOWLEDGMENTS

The authors would like to thank Dr. Stefanie Kaech Petrie, Dr. Crystal Chaw, Dr. Brian Jenkins, Dr. Felice Kelly, and Ms. Hannah Bronstein in the Advanced Light Microscopy at OHSU for technical and acquisition assistance with AxioScan.Z1 slide scanning microscopy studies. This work was funded by an ASPIRE Award from the Mark Foundation for Cancer Research (Gibbs) and R21CA257942 from the NIH/NCI (Gibbs).

## ■ REFERENCES

(1) Jiao, Q.; Bi, L.; Ren, Y.; et al. Advances in studies of tyrosine kinase inhibitors and their acquired resistance. *Mol. Cancer* **2018**, *17*, No. 36.
(2) Huang, L.; Jiang, S.; Shi, Y. Tyrosine kinase inhibitors for solid tumors in the past 20 years (2001−2020). *J. Hematol. Oncol.* **2020**, *13*, No. 143.
(3) Jain, R. K. Normalization of Tumor Vasculature: An Emerging Concept in Antiangiogenic Therapy. *Science* **2005**, *307*, 58−62.
(4) Chatterjee, S.; Wieczorek, C.; Schöttle, J.; et al. Transient antiangiogenic treatment improves delivery of cytotoxic compounds and therapeutic outcome in lung cancer. *Cancer Res.* **2014**, *74*, 2816−2824.
(5) Bottaro, D. P.; Liotta, L. A. Cancer: Out of air is not out of action. *Nature* **2003**, *423*, 593−595.
(6) Yu, H. A.; et al. Effect of Osimertinib and Bevacizumab on Progression-Free Survival for Patients With Metastatic EGFR-Mutant Lung Cancers: A Phase 1/2 Single-Group Open-Label Trial. *JAMA Oncol.* **2020**, 1048−1054.
(7) Li, H.; Takayama, K.; Wang, S.; et al. Addition of bevacizumab enhances antitumor activity of erlotinib against non-small cell lung cancer xenografts depending on VEGF expression. *Cancer Chemother. Pharmacol.* **2014**, *74*, 1297−1305.
(8) McMahon, N. P.; Solanki, A.; Wang, L. G.; et al. TRIPODD: a Novel Fluorescence Imaging Platform for In Situ Quantification of Drug Distribution and Therapeutic Response. *Mol. Imaging Biol.* **2021**, *23*, 650−664, DOI: 10.1007/s11307-021-01589-x.
(9) McMahon, N. P.; Solanki, A.; Wang, L. G.; et al. In situ single-cell therapeutic response imaging facilitated by the TRIPODD fluorescence imaging platform. *Theranostics* **2024**, *14*, 2816−2834.
(10) McMahon, N. P.; Jones, J. A.; Anderson, A. N.; et al. Flexible Cyclic Immunofluorescence (cyCIF) Using Oligonucleotide Barcoded Antibodies. *Cancers* **2023**, *15*, No. 827, DOI: 10.3390/cancers15030827.
(11) McMahon, N. P.; Jones, J. A.; Kwon, S.; et al. Oligonucleotide conjugated antibodies permit highly multiplexed immunofluorescence for future use in clinical histopathology. *J. Biomed Opt.* **2020**, *25*, No. 056004.
(12) Solanki, A.et al. *Intracellular Paired Agent Imaging Enables Improved Evaluation of Tyrosine Kinase Inhibitor Target Engagement*; Visualizing and Quantifying Drug Distribution in Tissue IV, SPIE, 2020.
(13) Wang, L. G.; et al. OregonFluor enables quantitative intracellular paired agent imaging to assess drug target availability in live cells and tissues. *Nat. Chem.* **2023**, No. 740, DOI: 10.1038/s41557-023-01213-1.
(14) Maeda, H.; Wu, J.; Sawa, T.; Matsumura, Y.; Hori, K. Tumor vascular permeability and the EPR effect in macromolecular therapeutics: a review. *J. Controlled Release* **2000**, *65*, 271−284.
(15) Tichauer, K. M.; Samkoe, K. S.; Sexton, K. J.; et al. Improved tumor contrast achieved by single time point dual-reporter fluorescence imaging. *J. Biomed. Opt.* **2012**, *17*, No. 066001.
(16) Tichauer, K. M.; Wang, Y.; Pogue, B. W.; Liu, J. T. Quantitative in vivo cell-surface receptor imaging in oncology: kinetic modeling and paired-agent principles from nuclear medicine and optical imaging. *Phys. Med. Biol.* **2015**, *60*, R239−269.
(17) Lin, J. R.; Wang, S.; Coy, S.; et al. Multiplexed 3D atlas of state transitions and immune interaction in colorectal cancer. *Cell* **2023**, *186*, 363−381.
(18) Pejovic, T.; Abate, P. V.; Ma, H.; et al. Single-Cell Proteomics Analysis of Recurrent Low-Grade Serous Ovarian Carcinoma and Associated Brain Metastases. *Front. Oncol.* **2022**, *12*, No. 903806.
(19) Labrie, M.; Li, A.; Creason, A.; et al. Multiomics analysis of serial PARP inhibitor treated metastatic TNBC inform on rational combination therapies. *NPJ. Precis. Oncol.* **2021**, *5*, No. 92.
(20) Li, A.; Keck, J. M.; Parmar, S.; et al. Characterizing advanced breast cancer heterogeneity and treatment resistance through serial biopsies and comprehensive analytics. *NPJ. Precis. Oncol.* **2021**, *5*, No. 28.
(21) Izar, B.; Tirosh, I.; Stover, E. H.; et al. A single-cell landscape of high-grade serous ovarian cancer. *Nat. Med.* **2020**, *26*, 1271−1279.
(22) Johnson, B. E.; Creason, A. L.; Stommel, J. M.; et al. An omic and multidimensional spatial atlas from serial biopsies of an evolving metastatic breast cancer. *Cell Rep. Med.* **2022**, *3*, No. 100525.
(23) Rozenblatt-Rosen, O.; Regev, A.; Oberdoerffer, P.; et al. The Human Tumor Atlas Network: Charting Tumor Transitions across Space and Time at Single-Cell Resolution. *Cell* **2020**, *181*, 236−249.
(24) Gray, G. K.; Li, C. C.; Rosenbluth, J. M.; et al. A human breast atlas integrating single-cell proteomics and transcriptomics. *Dev. Cell* **2022**, *57*, 1400−1420.
(25) Kim, T. Y.; et al. DNA Polymerase Alpha Subunit B Is a Binding Protein for Erlotinib Resistance in Non-Small Cell Lung Cancer. *Cancers* **2020**, *12*, No. 2613, DOI: 10.3390/cancers12092613.
(26) Nanthaprakash, T. V.; Gourlay, C. W.; Oehme, I.; et al. Phenotypic plasticity in a novel set of EGFR tyrosine kinase inhibitor-adapted non-small cell lung cancer cell lines. *FEBS Open Bio* **2025**, *15*, 1854−1873.
(27) Johnson, L. N. Protein kinase inhibitors: contributions from structure to clinical compounds. *Q. Rev. Biophys.* **2009**, *42*, 1−40.
(28) Eberhardt, J.; Santos-Martins, D.; Tillack, A. F.; Forli, S. AutoDock Vina 1.2.0: New Docking Methods, Expanded Force Field, and Python Bindings. *J. Chem. Inf. Model.* **2021**, *61*, 3891−3898.
(29) Wang, J.; Wang, W.; Kollman, P. A.; Case, D. A. Automatic atom type and bond type perception in molecular mechanical calculations. *J. Mol. Graphics Modell.* **2006**, *25*, 247−260.
(30) Jakalian, A.; Jack, D. B.; Bayly, C. I. Fast, efficient generation of high-quality atomic charges. AM1-BCC model: II. Parameterization and validation. *J. Comput. Chem.* **2002**, *23*, 1623−1641.
(31) Wang, J.; Wolf, R. M.; Caldwell, J. W.; Kollman, P. A.; Case, D. A. Development and testing of a general amber force field. *J. Comput. Chem.* **2004**, *25*, 1157−1174.
(32) Bussi, G.; Donadio, D.; Parrinello, M. Canonical sampling through velocity rescaling. *J. Chem. Phys.* **2007**, *126*, No. 014101.
(33) Darden, T. A.; Pedersen, L. G. Molecular modeling: an experimental tool. *Environ. Health Perspect* **1993**, *101*, 410−412.
(34) Genheden, S.; Ryde, U. The MM/PBSA and MM/GBSA methods to estimate ligand-binding affinities. *Expert Opin. Drug Discovery* **2015**, *10*, 449−461.

(35) Baker, N. A.; Sept, D.; Joseph, S.; Holst, M. J.; McCammon, J. A. Electrostatics of nanosystems: application to microtubules and the ribosome. *Proc. Natl. Acad. Sci. U.S.A.* **2001**, *98*, 10037−10041.
(36) Kumari, R.; Kumar, R.; Open Source Drug Discovery, C.; Lynn, A. g_mmpbsa–a GROMACS tool for high-throughput MM-PBSA calculations. *J. Chem. Inf. Model.* **2014**, *54*, 1951−1962.
(37) Abraham, J.; Nelon, L. D.; Kubicek, C. B.; et al. Preclinical testing of erlotinib in a transgenic alveolar rhabdomyosarcoma mouse model. *Sarcoma* **2011**, *2011*, No. 130484.
(38) Higgins, B.; Kolinsky, K.; Smith, M.; et al. Antitumor activity of erlotinib (OSI-774, Tarceva) alone or in combination in human non-small cell lung cancer tumor xenograft models. *Anticancer Drugs* **2004**, *15*, 503−512.
(39) Li, H.; et al. Nicotine induces resistance to erlotinib via cross-talk between alpha 1 nAChR and EGFR in the non-small cell lung cancer xenograft model. *Lung Cancer* **2015**, *88*, 1−8.
(40) Schöttle, J.; Chatterjee, S.; Volz, C.; et al. Intermittent high-dose treatment with erlotinib enhances therapeutic efficacy in EGFR-mutant lung cancer. *Oncotarget* **2015**, *6*, 38458−38468.
(41) Schürch, C. M.; Bhate, S. S.; Barlow, G. L.; et al. Coordinated Cellular Neighborhoods Orchestrate Antitumoral Immunity at the Colorectal Cancer Invasive Front. *Cell* **2020**, *182*, 1341−1359.
(42) Barua, S.; Solis, L.; Parra, E. R.; et al. A Functional Spatial Analysis Platform for Discovery of Immunological Interactions Predictive of Low-Grade to High-Grade Transition of Pancreatic Intraductal Papillary Mucinous Neoplasms. *Cancer Inf.* **2018**, *17*, No. 1176935118782880.
(43) Mund, A.; Coscia, F.; Kriston, A.; et al. Deep Visual Proteomics defines single-cell identity and heterogeneity. *Nat. Biotechnol.* **2022**, *40*, 1231−1240.
(44) Leighl, N. B.; Karaseva, N.; Nakagawa, K.; et al. Patient-reported outcomes from FLAURA: Osimertinib versus erlotinib or gefitinib in patients with EGFR-mutated advanced non-small-cell lung cancer. *Eur. J. Cancer* **2020**, *125*, 49−57.


https://doi.org/10.1021/acs.molpharmaceut.5c01220
*Mol. Pharmaceutics* 2026, 23, 1572−1585